PROMICE automatic weather station data

Robert S. Fausto[1], Dirk van As[1], Kenneth D. Mankoff[1], Baptiste Vandecrux[1], Michele Citterio[1], Andreas P. Ahlstrøm[1], Signe B. Andersen[1], William Colgan[1], Nanna B. Karlsson[1], Kristian K. Kjeldsen[1], Niels J. Korsgaard[1], Signe H. Larsen[1], Søren Nielsen[2], Allan Ø. Pedersen[1], Christopher L. Shields[1], Anne M. Solgaard[1], and Jason E. Box[1]

[1]The Geological Survey of Denmark and Greenland, Øster voldgade 10, 1350 København K, Danmark
[2]Deceased

Correspondence: Robert S. Fausto (rsf@geus.dk)

Abstract. The Programme for Monitoring of the Greenland ice sheet (PROMICE) has been measuring climate and ice sheet properties since 2007. Currently the PROMICE automatic weather station network includes 25 instrumented sites in Greenland. Accurate measurements of the surface and near-surface atmospheric conditions in a changing climate are important for reliable present and future assessment of changes of the Greenland ice sheet. Here we present the PROMICE vision, methodology, and each link in the production chain for obtaining and sharing quality-checked data. In this paper we mainly focus on the critical components for calculating the surface energy balance and surface mass balance. A user-contributable dynamic web-based database of known data quality issues is associated with the data products at (https://github.com/GEUS-PROMICE/PROMICE-AWS-data-issues/). As part of the living data option, the datasets presented and described here are available at DOI: 10.22008/promice/data/aws, https://doi.org/10.22008/promice/data/aws (Fausto et al., 2019).

1 Introduction

The ice loss from the Greenland ice sheet has contributed substantially to rising sea levels during the past two decades (Shepherd et al., 2020), and this loss has been driven by changes in surface mass balance (SMB) (Fettweis et al., 2017) as well as by solid ice discharge (Mouginot et al., 2019; Mankoff et al., 2020). SMB changes are typically assessed using regional climate models, but large uncertainties result in substantial model spread (e.g. Fettweis et al., 2020; Shepherd et al., 2020; Vandecrux et al., 2020). The spread is especially pronounced in regions of high mass loss (Fettweis et al., 2020). Obtaining in-situ measurements of accumulation and ablation and energy balance in the ablation area are therefore crucial for improving our understanding of surface processes. On-ice automatic weather stations (AWSs) have proven to be the ideal tool to perform such measurements (e.g. Smeets and Van den Broeke, 2008a; Fausto et al., 2016a). Presently, the PROMICE AWS data are not included in any reanalysis product such as ERA5, aiding studies with an independent assessment of the performance of regional climate models, and other numerical models that aim to quantify surface mass or energy fluxes (Fettweis et al., 2020).

The Geological Survey of Denmark and Greenland (GEUS) has been monitoring glaciers, ice caps, and the ice sheet in Greenland since the late 1970s (Citterio et al., 2015). Early projects involved ablation stake transects and automated weather

measurements (e.g. Braithwaite and Olesen, 1989), however, these efforts could not provide year-round measurements due to accessibility issues and technological limitations. The data these campaigns provided were therefore discontinuous in time and sparse in location. Monitoring programmes using AWSs operating year-round became achievable in the 1990s; the Greenland Climate Network (GC-Net) initiated at Swiss Camp in 1990 and extended to other sites in 1995 (Steffen et al., 1996) and in

5   1993 AWSs were installed on the K-transect along the southwestern slope of the ice sheet (Smeets et al., 2018). Recently, various institutions installed additional AWSs on the ice sheet, such as at Summit in 2008, and for the Snow Impurity and Glacial Microbe effects on abrupt warming in the Arctic (SIGMA) project in northwest Greenland in 2012 (Aoki et al., 2014). The majority of these AWSs are positioned in the accumulation area of the Greenland ice sheet. The ablation area of the ice sheet was monitored by a handful of stations, underlining the need for a long term monitoring programme for regions of the

10   ice sheet where melting is the largest mass balance component. Including the PROMICE AWSs in the low-elevation ablation area complements existing monitoring efforts and allows coverage in various climate zones of the ice sheet, which is necessary to improve understanding of spatiotemporal variability in the surface mass and energy components - key parameters for accurately assessing the state of the ice sheet.

15   In 2007, the Programme for Monitoring of the Greenland ice sheet (PROMICE) was initiated (Ahlstrøm et al., 2008; van As et al., 2011b). GEUS developed rugged AWSs equipped with accurate instruments, and placed them on the Greenland ice sheet and on local glaciers. The AWS design evolved over time with technological advances and lessons learned, but the aim remained to obtain year-round, long-term, and accurate recordings of all variables of primary relevance to the surface mass and energy budgets of the ice sheet surface. The PROMICE monitoring sites were selected to best complement the spatial

20   distribution of existing ice sheet weather stations, yet within range of heliports and airports.

The development of the PROMICE AWS started at GEUS in 2007 in collaboration with the GlacioBasis Programme monitoring the A.P. Olsen ice cap in northeast Greenland (APO), and the Greenland Analogue Project in southwest Greenland. The AWS is designed to endure extreme temperatures and winds, countless frost cycles, and an ever-changing snow/ice surface, but

25   with dimensions and weight allowing transportation by helicopter, snowmobile, and dogsled. The original PROMICE network consisted of 14 AWSs, with station pairs in seven regions: Kronprins Christian Land (KPC), Scoresbysund (SCO), Tasiilaq (TAS), Qassimiut (QAS), Nuuk (NUK), Upernavik (UPE) and Thule (THU). Per region the lower (L) station was placed near the ice sheet margin, and the upper (U) station higher up in the ablation area, closer to or at the equilibrium line altitude (ELA) where long-term mass gains and losses are in balance (Figure 1). Other projects collaborating with PROMICE led to the instal-

30   lation of 11 additional stations (Table 1). Currently some regions also include stations at for instance middle (M) or bedrock (B) sites. Three PROMICE AWSs are located in the accumulation area of the ice sheet (KAN_U, CEN and EGP), whereas two AWSs are on peripheral glaciers (NUK_K and MIT) not connected to the ice sheet. The PROMICE AWSs in Greenland transmit data by satellite in near real-time to support observational, remote-sensing and model studies; weather forecasting; local flight operations; as well as the planning of maintenance visits. The data have been important for quantifying ice sheet

35   change in e.g. annual international assessment reports such as the Arctic Report Card (Moon et al., 2020b) and the "State

of the climate" (Moon et al., 2020a). The data also proved crucial for calibrating, validating, and interpreting satellite-based observations and regional climate model ouput (Van As et al., 2014; Noël et al., 2018; Huai et al., 2020; Kokhanovsky et al., 2020; Solgaard et al., 2021).

The aim of this paper is to describe the PROMICE AWS dataset in detail. We discuss the measurement with insights into post-processing and sensor calibration. The dataset is freely available at www.promice.org (DOI:10.22008/promice/data/aws). We start with a description on how to construct the AWSs, followed by a technical description of the AWS instruments, the data production chain, examples of typical station measurements, and finally a summary and outlook.

2 The AWS design

2.1 The tripod

The AWS tripod is constructed from 32 mm (1.25″) and 44 mm (1.75″) radius aluminium tubes with 3 mm braided stainless steel wires forming a free-standing tetrahedral structure that connects legs and mast in a stable tripod (Figure 2). Most sensors are attached to the 1.7 m long horizontal boom, which is 2.7 m above surface (Figure 2). Weighing circa 50 kg, the battery box, is hanging under the mast to increase the mass of the AWS and to lower its center of gravity for better stability (Table 1). The tripod can easily be folded to fit in small helicopters. The tripod can also be tilted during maintenance visit for e.g. sensor replacement. Because the tripod is standing freely on the ice surface, it sinks with the melting surface, which results in sonic ranger measurements on the AWS do not capture ice melt. Therefore each PROMICE AWS on ice is accompanied by a separate sonic ranger stake assembly constructed from 32 mm aluminum tubing, typically drilled 7 m into the ice that does not float with on the ice (Figure 2).

2.2 Instrumentation and data transmission

The PROMICE AWS measures 1) the meteorological parameters required for calculating the surface energy budget, 2) snow ablation/accumulation and ice ablation, 3) sub-surface temperature at 8 depths (Thermistor string, Figure 2), and 4) position by GPS. The next section provides details on the frequency and accuracy of measurements taken by each sensor. Further sensor details are provided in the Appendix.

Measurements are taken every 10 minutes and stored in the data logger locally. The AWSs transmit hourly averages based on 10-minute measurements during the period with ample solar power, between day-of-year 100 and 300 (10 April and 26 October in non-leap years). Exceptions are parameters with low variability (GPS position, station tilt, surface height, etc.) that are transmitted less frequently (every 6 hours) in order to reduce transmission cost. In winter, between day-of-year 300 and 100, the stations only transmit daily averages of all parameters to limit power consumption by the satellite modem. Transmission is done through the Iridium satellite network that has coverage even at the northernmost latitudes. The Iridium short

burst service transmits up to 340 bytes per message. The program running on the data logger ensures a correctly transferred data string from the logger to the transmitter if an Iridium satellite is in view. In case of no successful transmission through the satellite the logger program will try again. Depending on the availability of the Iridium service the logger program can also queue the message for delivery at a later time with better satellite connection. This relatively low power operation mode ensures unnecessary transmission attempts with a low rate of message loss. Moreover, the logger program encodes the data in a binary format before transmission, which reduces the size of the message and by that transmission costs with about 2/3.

To ensure reliable and accurate measurements, instruments in the field are swapped following an instrument maintenance schedule based on information from manufacturers and from experience, for instance with battery life and performance, when charging batteries without a charge regulator. The maintenance schedule is a guideline; not always does a field crew return to an AWS in time for a scheduled sensor swap. For example, we only visit the AWSs in the north-eastern part of Greenland (KPC, Figure 1) every 3-4 years as their remoteness weighs heavily on the logistics budget. Thankfully, the most remote PROMICE AWSs experience less melt, lower accumulation and weaker storms than some other places, reducing the need for maintenance visits. Maintenance visits typically take 2-4 hours, which include replacing sensors scheduled for recalibration, re-drilling installed sensors in ice, and occasional repairs.

3 Measurements

3.1 Dataset pruduction chain

PROMICE AWS data are processed by the production chain algorithm with some manual expert quality checking twice a year (typically in January and after the summer), and in real time with automated quality check in the PROMICE database. For our production chain algorithm, we make use of the raw data recorded every 10 minutes, retrieved from the data logger during maintenance visits (Figure 3). For the period since the last station visit we use the transmitted data for the PROMICE data products. Beside the direct AWS measurements, we also calculate certain variables based on these measurements, for instance tilt-corrected solar radiation and turbulent heat fluxes. In the following, we describe each variable in the PROMICE AWS dataset, and how it is measured or derived. We refer to the manufacturer specific instrument information, accuracy, and power consumption (see Table 2 and sensor specific tables in Appendix). We use simple thresholds on 10-min data to remove spikes and inconsistent or bad measurements (see section "Post processing" below for more information). Available transmitted data are used for filling in data gaps.

3.2 Measured variables: description and uncertainty

For most measured variables, the data logger converts readings in voltage to physical values using simple scaling relations with calibration coefficients specific for each instrument. Only when identical sensors can have different calibration coefficients, namely the radiometer and pressure transducer, the conversion from voltage is done in post-processing; the advantage being

that a sensor swap does not require a data logger program change in the field. Below, we mention all scaling relations needed to manually convert logger data to physical measurements.

Air pressure

Barometric pressure (unit: hPa) is measured in the fiberglass-reinforced polyester logger enclosure (Figure 2, number 9). The logger enclosure is generally located 1.5 m above the ice surface. The barometer manufacturer reports a measurement accuracy of ±2 hPa within the -40 to +60 °C temperature range (Table 2, see also Appendix for more information).

Air temperature

Air temperature (unit: °C) is measured inside a fan-aspirated radiation shield (Figure 2, number 6). The sensor is located approximately 2.6 m above the ice surface, i.e. as high as possible underneath the sensor boom. The measurement height varies when a winter snow cover is present. The temperature sensor is a PT100 probe that changes its electrical resistance with temperature and has an accuracy of ±0.1 °C (Table 2, see also Appendix for more information). Also a secondary air temperature reading (°C) is made in the aspirated shield from the Hygroclip temperature/humidity sensor described in the following, also with a manufacturer stated accuracy of ±0.1 °C, but we consider the Hygroclip temperature to be less accurate than the PT100, given the need for more frequent sensor re-calibrations.

Humidity

Relative humidity (RH) (unit: %) is measured alongside the PT100 in the aspirated radiation shield using a HC2A-S3 (or HC2) "Hygroclip" (Figure 2, number 6). The sensor measures relative humidity with ±0.8 % accuracy. Relative humidity is measured relative to water. For temperatures below freezing, relative humidity is recalculated relative to ice in post-processing (see section 3.3). To distinguish between the two relative humidities in the PROMICE data products, the prior humidity (unadjusted below freezing) is called "relative humidity with respect to water", while the latter simply is "relative humidity". The conversion of relative humidity relative to ice is after Goff and Gratch (1946). Every 1-2 years, the Hygroclip is replaced by a sensor re-calibrated in a closed chamber at room temperature with constant relative humidities of 10, 35, 80 %.

Wind speed and direction

Wind speed and direction (Units: m s^{-1} and °) measurement height is approximately 3.1 m above the ice surface, and like the other measurements has a reduced measurement height in case a winter snow layer is present (Figure 2, number 4). An AC sine wave voltage signal is produced by the rotation of the four-bladed propeller, and the pulse count converts to wind speed using a multiplier. According to the manufacturer the sensor can measure wind speeds between 0 and 100 m s^{-1}, with an accuracy of ±0.3 m s^{-1} or 1% if the measured value is higher than 30 m s^{-1}.

Wind direction is measured through changes in the vane angle by a precision potentiometer housed in a sealed chamber on the

instrument. The output voltage is directly proportional to vane angle wind direction is measured between 0 - 360° with an accuracy of ±3°. Every three years the sensor is replaced and tested for drift and functionality with an "anemometer drive" rotating the propeller at a known rate. The instrument's orientation is logged and reset to "Geographic north" during each maintenance visit to keep wind direction data accurate within ±15° (although much larger station rotations have been encountered).

5 Upward and downward shortwave radiation

Horizontally-leveled up and down facing Kipp & Zonen CNR1 or CNR4 record solar radiation (units: W m^{-2}), respectively. Measurement height is at the sensor boom level of 2.7 m over the ice surface (Figure 2, number 1). Shortwave radiation is measured by the pyranometers within plastic meniscus domes, allowing minimal water droplet adhesion. The manufacturer reports that sensor uncertainty is 10%. This sensor uncertainty has in practice been found to be ca. 5% for daily totals in Antarctica ((van den Broeke et al., 2004)). The radiometers are recalibrated at Kipp & Zonen every three years. The radiometer is one of the few variables stored in the data logger in voltage (V) units, because every radiometer has a different set of calibration coefficients, whereas all logger programs running on PROMICE AWSs are identical, for practical reasons. In postprocessing, sensor readings SR_{raw} are converted into a physical measurement SR_m following:

$$SR_m = \frac{SR_{raw}}{C_{SR}}, \tag{1}$$

where C_{SR} (unit: $V(Wm^{-2})^{-1}$) is a sensor calibration coefficient and SR_m is either the converted downward and upward shortwave irradiance. Shortwave radiation measurements are corrected for sensor tilt following van As et al. (2011a) in postprocessing, which means that the PROMICE AWS dataset contains both uncorrected and corrected values.

Upward and downward longwave radiation

Longwave radiation (units: W m^{-2}) is also measured by the CNR1/CNR4 radiometer mounted at approximately 2.7 m over the ice surface (Figure 2, number 1). The radiometer contains a pair of up- and downfacing pyrgeometers, with a spectral range of 4.5 to 42 μm. As for shortwave radiation, longwave radiation is stored in voltage units (LR_{raw}) in the data logger, and transformed to physical units (LR_m) in post-processing following:

$$LR_m = \frac{LR_{raw}}{C_{LR}} + 5.67 \cdot 10^8 \cdot (T_{rad} + T_0)^4, \tag{2}$$

where C_{LR} (unit: $V(Wm^{-2})^{-1}$) is the sensor calibration coefficient. T_{rad} is the sensor temperature measured in the radiometer casing in °C and $T_0 = 273.15$ °C.

Surface height

The height of the sensor boom (units: m) is measured by a sonic ranger attached to the boom itself attached approximately 0.1 m below the boom (Figure 2, number 5a), while the height of the stake assembly is measured about 0.1 m below an aluminum boom connecting stakes drilled into ice (Figure 2, number 5b). The sensor outputs a distance (H_{raw}) that requires an air

temperature correction in post-processing. The temperature adjustment is performed following:

$$H_m = H_{raw} \cdot \sqrt{\frac{T_{air} + T_0}{T_0}} \tag{3}$$

After temperature correction, the measurement uncertainty of the SR50A sonic ranger reported by the manufacturer (Campbell Scientific) is ± 1 cm or ± 0.4 % of the measured distance. The uncertainty of sonic ranger readings in PROMICE was investi-

5   gated utilizing data from a wintertime accumulation-free period of more than 2 month at the location SCO_U. The associated standard deviations for the two sensors were found to be 1.7 cm and 0.6 cm after spike removal, amounting to 0.7 % and 0.6 % of the measured distance, respectively ((Fausto et al., 2012)). In addition to the sensor uncertainties, occasional problems with the stake assembly occurred, primarily in terms of stability during storms when melted out several meters. Also, an unknown amount of melt-in of the stake assembly can occur, but we speculate this only happens 1) when surface melt since installation

10 has been considerable, increasing the height of and thus pressure applied by the stake assembly, and 2) when the stake bottoms are not plugged with caps, as was only the case until 2010.

The PROMICE AWSs are also equipped with a pressure transducer assembly (PTA) that measures surface height change due to ice ablation (Figure 2, number 7). The assembly was first constructed and implemented in Greenland in 2001 by Bøggild et al. (2004), but was further developed within PROMICE (Fausto et al., 2012). The PTA consists of an 50/50 antifreeze/water

15 mixture filled hose with a pressure transducer attached at the bottom. Drilling the hose typically more than 10 m into the ice, the pressure signal registered by the transducer will be that of the vertical liquid column over the sensor, where the upper level is a bladder fixed on the tripod in a shielded box. This allows in-/outflow of antifreeze due to compression while keeping a steady level at roughly 1.5 m above the ice surface depending on the AWS. Figure 2 illustrates the free-standing AWS tripod that floats on the ice surface and moves down with the ablating surface, while the hose itself melts out of the ice, which in

20 turn will reduce the hydrostatic pressure from the vertical liquid column over the pressure transducer at the bottom of the hose. The measured reduction in pressure at the bottom of the hose translates directly into ice ablation. As for the radiometer, every pressure transducer has a different calibration coefficient, which is why measurements are stored in the data logger in voltage units and transformed to a physical measurement in post-processing. Measurement height (H_m), or in fact depth relative to the PTA bladder, is calculated as follows:

$$H_m = C_{PTA} \cdot \frac{\rho_w}{\rho_{af}} \cdot H_{raw}, \tag{4}$$

where C_{PTA} is the calibration coefficient. The constants ρ_w and ρ_{af} are the densities of water and the 50/50 antifreeze/water solution, respectively.

Sub-surface temperature

Subsurface temperatures (unit: °C) are measured by a 10 m thermistor (temperature-dependent resistor) string (Figure 2, num-

30 ber 11). The string measures at 1, 2, 3, 4, 5, 6, 7 and 10 m depth, although depths vary due to the surface ablation and accumulation. The string is constructed at GEUS (see Appendix for more information).

Station tilt

The inclinometer is installed on the sensor boom (Figure 2, number 2) and is aligned with the radiometer to allow for tilt correction of shortwave radiation measurements. The inclinometer measures the tilt (unit: °) across (left-right) and along (up-down) the sensor boom, which translates into tilt-to-east and tilt-to-north when the sensor boom is perfectly oriented

5   north-south. The tilt sensor readings in voltage units ($Tilt_{raw}$) are converted into tilt in degrees following:

$$Tilt_m = 21.1 \cdot |Tilt_{raw}| - 10.4 \cdot |Tilt_{raw}|^2 + 3.6 \cdot |Tilt_{raw}|^3 - 0.49 \cdot |Tilt_{raw}|^4, \tag{5}$$

where all constants were determined at GEUS (Table 2). Ice ablation causes the AWS tripod to melt downward; this changing (slippery) surface often results in AWS tilt changes of more than several degrees.

AWS position

10   We use a single frequency GPS receiver to measure the position (units: °N/°W) and the elevation (unit: m above sea level) of each station to quantify ice flow velocity (Figure 2, number 9). The GPS antenna, as well as the receiver which is contained in the Iridium modem, is placed inside the data logger enclosure. It is a single frequency GPS, which is built into Iridium 9602-LP modem. The receiver type is a NEO-6Q, 1575.42 MHz (L1), 16-channel, with a C/A code. The accuracy is reported to be within 2.5 m. In the PROMICE AWS setup, the GPS receiver is powered up for 5 minutes preceding each Iridium transmission

15   (hourly in summer and daily in winter), during which it attempts to acquire location data every 20 seconds. The return (out of a maximum of 15) that reports the lowest horizontal dilution of precision is written to memory. So far, NUK_U, NUK_L, MIT and QAS_L have been repositioned during maintenance visits over distances larger than several tens of meters. The main reason for this is to reduce the influence of location change on the AWS variables measured, but stations have also been relocated to move them away from a region with opening crevasses. Table 4 shows the horizontal and vertical displacement

20   due to glacier flow and AWS relocation during maintenance visits.

3.3   Post-processing

In this section, we describe and quantify the filtering process, how we correct measurements, and how we calculate derived variables in the dataset. The hourly, daily, and monthly averaging procedures are also described.

3.3.1   Filtering

25   Table 5 provides filtering information used in the processing chain. We remove unrealistic spikes from the data by using upper and lower thresholds for each measurement. Measurements outside these (generous) threshold limits, which could happen for a number of known and unknown reasons, are considered erroneous and set to -999. Known reasons will be discussed in section 4.3 (Living data section). Derived variables are also set to -999 when one or more of the listed "core" AWS measurements that serve as input fall outside the threshold limits.

3.3.2 Derived and corrected variables

Specific humidity

The specific humidity q (unit: kg/kg) is calculated from relative humidity with respect to water/ice above/below freezing (RH) using the following equation:

$$q = \frac{RH}{100} \cdot q_{sat}, \tag{6}$$

with

$$q_{sat} = \frac{\epsilon \cdot es_{ice/water}}{p - (1 - \epsilon) \cdot es_{ice/water}}, \tag{7}$$

where $\epsilon = 0.622$ is the ratio between the specific gas constants for dry air and water vapor, p is air pressure in Pa and $es_{ice/water}$ is saturation water vapor pressure over ice in Pa (below freezing) or water (above freezing) calculated after Goff and Gratch (1946).

Surface temperature

The surface temperature T_s (unit:C) is derived using the measured downward and upward longwave irradiance (LR_{in} and LR_{out}, respectively):

$$T_s = \left(\frac{LR_{out} - (1 - \epsilon) \cdot LR_{in}}{\epsilon \cdot 5.67 \cdot 10^{-8}} \right)^{0.25} - 273.15, \tag{8}$$

where ice sheet surface emissivity $\epsilon = 0.97$.

Turbulent energy fluxes

The sensible (SHF) and latent (LHF) heat fluxes (unit: W m^{-2}) are estimated using vertical gradients in wind speed, potential temperature, and specific humidity between the measured boom height and the surface described by Van As et al. (2005); Van As (2011). According to the Monin-Obukhov similarity theory, SHF and LHF can be approximated as:

$$SHF = \rho C_p \kappa^2 \frac{u}{ln\frac{z_u}{z_0} - \psi_u} \frac{T - T_s}{ln\frac{z_T}{z_{0,T}} - \psi_T}, \tag{9}$$

$$LHF = \rho L_{s/v} \kappa^2 \frac{u}{ln\frac{z_u}{z_0} - \psi_u} \frac{q - q_s}{ln\frac{z_q}{z_{0,q}} - \psi_q}, \tag{10}$$

Here ρ is the density of air and $C_p = 1005 \ JK^{-1}kg^{-1}$ its specific heat capacity at constant pressure. $L_s = 2.83 \cdot 10^{-6} \ Jkg^{-1}$ and $L_v = 2.50 \cdot 10^{-6} \ Jkg^{-1}$ are the latent heat values of sublimation and evaporation, respectively, while $\kappa = 0.4$ is the von Karman constant. When estimating turbulent heat fluxes, we need the measurement heights (z_u, z_T, z_q, Table 2) of wind speed (u), temperature (T), and specific humidity (q) as well as the surface roughness lengths for momentum z_0, for heat, $z_{0,T}$ and moisture $z_{0,q}$. We use $z_0 = 0.001$ m and $z_{0,T} = z_{0,q}$ is calculated using the formulation from Smeets and Van den Broeke (2008a, b) for rough surfaces. We use the stability correction functions $\psi_{u,T,q}$ from Equation 12 in Holtslag and De Bruin (1988) for stable atmospheric conditions, while we follow Paulson (1970) for unstable conditions. The surface temperature

(T_s) is calculated from longwave radiation (see Eq. (8)) and the surface specific humidity is assumed to be at saturation $(q_s = q_{sat})$.

Several sources of uncertainty apply to the calculation of SHF and LHF. The aerodynamic surface roughness length z_0 is known to vary with surface type (Brock et al., 2006) and through time (Smeets and Van den Broeke, 2008a, b). Using the constant value of $z_0 = 0.001$ m could be an overestimation of surface roughness in presence of snow and subsequently lead to an overestimation of both turbulent fluxes. Since most PROMICE stations are located in the ablation area, the snowpack is melted during spring and the surface becomes snow-free for most of the ablation season. The calculation of surface temperature also relies on certain assumptions (see section above). Several studies evaluated the performance of the Monin-Obukhov similarity theory in Greenland. Using two and single profile level methods versus eddy covariance and evaporation lysimeters, Box and Steffen (2001) found underestimation of downward LHF during extreme stability cases. Miller et al. (2017) used a similar method for calculating SHF and reported a root mean square difference (RMSD) of $8.7\ Wm^{-2}$, with average bias of $-7.0\ Wm^{-2}$, when compared with their two-level Eddy Covariance estimation of SHF. Miller et al. (2017) emphasized that SHF records by one-level approaches often cover longer time periods. Fausto et al. (2016a, b) investigated the use of an unrealistically high z_0 to get agreement between SEB closure and observed ablation rates during extreme sensible and latent heat-driven melt events.

Tilt correction of downward shortwave radiation and Cloud Cover

Tilt correction of solar radiation is performed following Van As (2011). Downward shortwave radiation (SR_{in}) consists of a diffuse and direct beam part. It is only the direct beam part of SR_{in} that requires tilt correction. For a horizontal radiation sensor, the direct beam, which equals SR_{in}, is reduced by its diffuse fraction (f_{dif}). For the tilted radiation sensor, SR_{in} is calculated from the measured value, $SR_{in,m}$ and a correction factor C following:

$$SR_{in,cor} = SR_{in,m}\frac{C}{1 - f_{dif} + Cf_{dif}}, \tag{11}$$

with

$$C = \cos(SZA) \cdot \Big(\sin(d)\sin(lat)\cos(\phi_{sensor}) - \sin(d)\cos(lat)\sin(_{sensor})\cos(\phi_{sensor}) +$$

$$\cos(d)\cos(lat)\cos(\theta_{sensor})\cos(w) +$$

$$\cos(d)\sin(lat)\sin(\theta_{sensor})\cos(\phi_{sensor})\cos(w) + \cos(d)\sin((\theta_{sensor})\sin(\phi_{sensor})\sin(w) \Big)^{-1} \tag{12}$$

where SZA is the solar zenith angle, d is the sun declination (the angle of the sun above the plane formed by the earth's equator), w is the hour angle (the angle between the sun's current position in the sky and its position at solar noon), lat and lon are the site's latitude and longitude in radians, and lastly θ_{sensor} and ϕ_{sensor} are the radiometer's tilt angle and direction, respectively. The calculation procedures for d and w and SZA are detailed in (Vignola, 2019). Table 3 illustrates the average bias

or correction made for the incoming solar radiation based on Equation (11). The standard deviation indicates for most AWSs that the average correction is minor (below 15 Wm^{-2}), while few AWSs have corrections values spread out over a wider range.

We estimate f_{dif} spanning from 0.2 for clear skies to 1 for overcast conditions, while assuming a linear dependency on the cloud cover fraction (Harrison et al., 2008). We approximate the cloud cover fraction from its dependence of the near-surface air temperature (T_{air}) on LR_{in} (Van As et al., 2005). For this purpose, we calculate a theoretical downward longwave radiation flux corresponding to clear sky conditions using the equation from Swinbank (1963):

$$LR_{clear} = 5.31 \cdot 10^{-14} \cdot (T_{air} + T_0)^6, \tag{13}$$

and to overcast conditions assuming the black-body radiation:

$$LR_{overcast} = 5.67 \cdot 10^{-8} \cdot (T_{air} + T_0)^4. \tag{14}$$

The cloud cover (limited to the [0:1] range) is then calculated as:

$$cloudcov = \frac{LR_{in} - LR_{clear}}{LR_{overcast} - LR_{clear}} = \frac{f_{dif} - 0.2}{0.8} \tag{15}$$

Albedo

Surface broadband solar reflectivity in the 0.3 to 2.5 μm wavelength range, a.k.a., albedo (unitless) is calculated from 10 minute tilt-corrected downward and upward solar irradiance data. Hourly averaged albedo values are calculated for cases when the sun hits the radiometer top in angles exceeding 20, i.e. when measurements are most reliable for this sensor type. Daily albedo averages are computed from available hourly data. AWS obstruction of sunlight, casting a shadow within the radiometer's field of view, may lower the albedo on average by 0.03 (Kokhanovsky et al., 2020), but depends on surface type and height. Also of relevance to measured albedo is the contrast of the surface relative to the AWS battery box, legs, mast and enclosure, and whether a melt pond forms beneath the AWS. Ryan et al. (2017) examined spatial variograms in UAV-derived albedo versus satellite and PROMICE albedo and found differences increasing for some PROMICE sites toward the late melt season when the AWS point measurements lack representativity of the increasingly inhomogeneous surface cover. van den Broeke et al. (2004) found a 5% uncertainty on pyranometer measurements, while the manufacturer, Kipp & Zonen, estimates a more conservative value of 10% uncertainty. We conservatively assume 10 % uncertainty in the calculated albedo.

Ice surface height

The pressure transducer assembly (PTA, Figure 2, sensor 7) setup is influenced by variations in air pressure. The air pressure contributions to the measured PTA signal H_M are eliminated using the following equation:

$$H_L = H_M + \frac{P_C - P_A}{g\rho_l}, \tag{16}$$

where P_A (Unit: hPa) is air pressure, P_C (Unit: hPa) is the known pressure given by the manufacturer to which the sensor was calibrated, $g = 9.82$ m s^{-2} is the gravitational acceleration, and $\rho_l = 1090$ kg m^{-3} is the antifreeze mixture density at 0 °C.

Changes in H_L are equal to ice ablation. Fausto et al. (2012, 2016a) compared PTA time series to hose measurements manually performed in the field and recorded distances from sonic rangers to quantify instrument inaccuracies, which were found to be accurate within 0.04 m.

3.3.3 Averaging

The time reported in our data products specifies the hour/day/month during which the measurements are taken, as opposed to other products that list the exact timestamp of the end of the averaging period. Hourly averages are calculated from 10-min values if at least one value is available (10-minute data are seldomly missing). We then calculate daily averages from hourly averages if at least 20 values ($\sim$80%) are available for a dataset variables with a clear diurnal variability. Less transient variables require at least one measurement to calculate an average. Lastly, we calculate the monthly averages from daily averages if at least 24 values ($\sim$80%) are available.

3.3.4 Measurement success rate

To illustrate the PROMICE AWS data coverage, we determined the "success rate" in terms of available daily averages for all measured variables that are required for estimating the surface energy budget: air pressure, air temperature, humidity, wind speed, and down- and upward short- and longwave radiation. Success rate is defined as the ratio of the counts of not-flagged and the number of days since AWS installation. The performance for the critical variables for each station and their measurement periods is illustrated in Figure 4. Eighteen out 26 stations have at least a 85% success rate for all critical surface energy budget variables, while six have experienced significant periods with power failure, station toppling, snow accumulation exceeding instrument height, or even crevasse formation underneath the station.

4   Data products and availability

The PROMICE AWS data are made available in hourly (H), daily (D), and monthly (M) time resolutions. The data products include variables listed in Table 6. The data are organised in ASCII files, organized following Table 6, with 46 columns in the hourly datafiles, 45 columns in the daily datafiles, and 24 columns in the monthly datafiles. The datafiles can be accessed through "Download Data" on the PROMICE webpage https://www.promice.org (DOI: 10.22008/promice/data/aws).

4.1   Data climatology: Average and standard deviation

Here, we make a short presentation of meteorological variables and the surface energy balance components based on the daily data product. Table B1 shows the average and standard deviation for all available dataset variables for the period 2008-2020. In general, Table B1 illustrates that the shortwave radiative fluxes vary from 118.0 $\pm$ 134.2 at KPC_L in the north to 130.2 $\pm$ 111.2 at QAS_L in the south depending mainly on cloud cover and season. Stations at higher elevation tend to get more sunlight than the lower lying stations(van As et al., 2013; Fausto et al., 2016b). The turbulent fluxes (sensible and latent heat) shows a positive contribution from the sensible heat flux and a negative contribution from the latent heat flux both with a

considerable variation. The turbulent fluxes are on average lower in magnitude than the radiative fluxes and tend to be higher at lower latitudes and elevation (Fausto et al., 2016b). The temperature is generally higher for stations located at lower elevations close to the ice-sheet margin, because they are more exposed to the relatively warm atmospheric conditions of the ocean all year round, except for stations at higher latitudes (above 70 N), which experience sea ice condition during winter influencing the temperature (van As et al., 2011a, 2014). Table B1 also illustrates that the temperature has a clear dependence on latitude and elevation. On average, the wind speed tends to increase with elevation, which is mainly due to the surface radiative cooling during winter (van As et al., 2014).

4.2 Data examples

To create a quick insight into the data product, we show examples of data from AWSs in two contrasting locations: TAS in southeast Greenland near Tasiilaq and UPE in northwest Greenland near Upernavik (Figure 1).

4.2.1 Wind speed

Time series spanning the years 2012 through 2014 of weekly median wind-speeds and maximum 10-min wind speed within that week for TAS_L and UPE_U are displayed in Figure 5. Median wind speeds are lower at TAS_L than at UPE_U, whereas the opposite is true for maximum wind speeds, because TAS_L is located in a region well-known for its piteraq storms.

4.2.2 Air temperature

The daily average air temperature for the two stations near Upernavik is shown in Figure 6. The temperature is higher at the lower station, UPE_L, than at the upper station, UPE_U due to an elevation difference of more than 700 m. The tendency of the temperature to have a higher variability during winter months than during summer is also evident from these time series.

4.2.3 Surface energy balance

Figure 7 presents the surface energy fluxes at UPE_U in 2012. The plots show how UPE_U experiences a shorter period with solar radiation, due to the more northerly location, when comparing to the TAS stations further south. Furthermore, Figure 7 shows how the outgoing longwave radiation becomes stable during the main melt season when the surface temperature is at the melting point. The sum of all the fluxes determines if there is a surplus of energy at the surface, which can be used for snow or ice melt.

4.3 Living data and continuing improvements

PROMICE will continue to update and make available the data products as AWS data comes in. It is likely that there are as-yet-unknown issues in the existing data we are releasing as part of this dataset, and new issues may arise in as-yet-to-be collected data. Also, some issues are known but hard to identify and some issues are systematic, which can be corrected for more generally. Below, we list known dataset issues in three categories: 1) Issues that are hard to identify 2) issues we in some

way can correct for systematically, and 3) Errors caused by humans, animals, and anything due to instrument failure.

Here, we list dataset issues we have encountered over the years following the above three categories:

1. Hard to identify

   (a) Often a high inclinometer variability, presumably caused by AWS shaking, or instrument failure.

   (b) Riming affecting several measured variables.

   (c) Undocumented AWS orientational drift.

   (d) Sonic ranger membrane not robust enough to always survive the period between maintenance visits (instrument failure).

   (e) Instruments buried in snow during winter and/or spring.

   (f) Tripod collapse due to compacting snow.

   (g) AWS falling over in extreme winds or crevassed terrain.

   (h) Bent sensor boom due to compacting snow, impacting alignment radiometer and inclinometer.

   (i) Leaks in or overfilling of the pressure transducer assembly.

   (j) Static electricity by snow drift or damage to the AWS's electrical circuit.

2. Systematic correction

   (a) Radiometer sensor tilt (we already correct for this).

   (b) Glacial movement causing gradual changes in AWS positions and thereby their measured variables

   (c) Shading by instruments and station frame impacting measurements, e.g. albedo.

3. Errors caused by humans and animals

   (a) Human error, such as sensor plug swap during maintenance visits or improper (wrong height/orientation) sensor mounting.

   (b) Animal occasionally soiling instruments and AWS surroundings.

   (c) Various instrument failures.

The most recent data files will in most cases comprise of transmitted data, which will be updated after the next maintenance visit. Data download from the logger will improve data quality and coverage. During strong winds the AWSs can topple or sensors break down. AWSs can also be covered by winter-accumulated snow, in which cases will reduce the data quality for many variables. We can with our height measurements on both the station and stake assembly monitor when certain instruments are covered in snow. At present, AWS covered in snow has only happened at three locations, namely QAS_U, QAS_M and

MIT. Data recorded after and during these events are often identified by the automatic processing routine and will be clearly identifiable for the data user as erroneous data. A maintenance visit either in spring or summer will often result in a station being moved, leveled, and/or rotated, in which case variables such as surface height will undergo an easily recognizable shift.

5 Identified dataset issues that we plan to correct for or implement in future data products:

1. Shading by instruments and station frame impacting albedo.

2. Instrumental monitoring of AWS orientation, which could influence the correction of the shortwave radiation and wind direction.

3. Instrumental monitoring of rain.

10 4. Flagging protocol for identified errors and issues.

While we do our best to clean the data appropriately and address known issues (see above), we recognize that correcting issues is more complicated than simply documenting them, and that some corrections may not be possible, or may be subjective and a function of different use cases. We therefore introduce a user-contributable dynamic web-based database of known data quality issues at (https://github.com/GEUS-PROMICE/PROMICE-AWS-data-issues/). The current implementation uses

15 GitHub "issues", although a future version may use a different database backend that the DOI would resolve. Each issue is tagged with station(s), sensor(s), and year(s) where the issue occurs. Users who are working with a station, sensor, or time-frame of data are encouraged to search the issue database and see if there are any known relevant data issues. If users discover a data issue that is not currently documented, they can add it to the database. A PROMICE team-member will review and tag any issues as verified, and then suggest a fix. Future versions of the product will implement these fixes if possible, and the

20 issues will be closed but remain accessible.

5   Summary and outlook

The UN Inter-Governmental Panel on Climate Change (IPCC) has previously highlighted the value of station-level records for assessing the cryospheric changes associated with global climate change (Vaughan et al., 2013). The IPCC has more recently highlighted the importance of understanding Greenland ice sheet mass loss, especially mass loss due to atmospheric forcing

25 and surface mass balance mechanisms, as a leading contributor to sea-level rise (Meredith et al., 2019). Meteorological and glaciological monitoring sites on the ice sheet are necessary to provide well-constrained observations of surface energy and mass balances. Understanding these local energy and mass balances provides the process-level knowledge of ice sheet and atmosphere interactions required by regional and global simulations (e.g. Van As, 2011; Fausto et al., 2016b). The PROMICE network plays a leading role in providing these in situ observations and process-level insights for the Greenland ice sheet.

30 The PROMICE AWS v3 data products are made available as hourly, daily, and monthly datafiles. All data products undergo periodical improvement through updates in the processing chain. Data are added as they are received from field parties and

through satellite transmission. Between 2007 and 2021, the PROMICE AWSs have measured with a success rate of 85% for 18 out of 26 stations, defined as the availability fraction of the daily averages for variables required for calculating the surface energy balance (see Figure 4). All PROMICE AWS data products are available at https://doi.org/10.22008/promice/data/aws.

In addition to advancing science, the PROMICE AWS network is now poised to contribute to operational products. With recent advances in the quality and transparency of the PROMICE data delivery pipeline described here, as well as the increasing prevalence of machine-to-machine transfer protocols among data users, the entire PROMICE station data archive – including near real-time observations – is now readily available to ingest in weather forecast and climate reanalysis applications. With the original AWS stations quickly approaching its fifteenth anniversary, the PROMICE data record is crossing the halfway mark of a thirty-year climatological reference period. With the launch of the PROMICE AWS data issues on GitHub (https://github.com/GEUS-PROMICE/PROMICE-AWS-data-issues/), we hope to continue to support the growing PROMICE user community into the next decade.

6 Data availability

The PROMICE AWS product has DOI: https://doi.org/10.22008/promice/data/aws. Fausto et al. (2019) is the dataset citation.

Author contributions. RSF and DVA produced the PROMICE AWS product. RSF and KDM set up the data-curation framework. RSF prepared the manuscript with contributions from all co-authors, except SN who is deceased.

Competing interests. Authors declare that they have no conflict of interest.

Acknowledgements. AWS data from the Programme for Monitoring of the Greenland ice sheet (PROMICE) and the Greenland Analogue Project (GAP) were provided by the Geological Survey of Denmark and Greenland (GEUS) at https://www.promice.org. We would like to thank the editor, David Carlson, one anonymous reviewer and Jacob C. Yde for their thoughtful comments and suggestions.

References

Ahlstrøm, A. P., Gravesen, P., Andersen, S. B., van As, D., Citterio, M., Fausto, R. S., Nielsen, S., Jepsen, H. F., Kristensen, S. S., Christensen, E. L., Stenseng, L., Forsberg, R., Hanson, S., and Petersen, D.: A new programme for monitoring the mass loss of the Greenland ice sheet, Geological Survey of Denmark and Greenland Bulletin, 15, 61–64, 2008.

5   Aoki, T., Matoba, S., Uetake, J., Takeuchi, N., and Motoyama, H.: Field activities of the "Snow Impurity and Glacial Microbe effects on abrupt warming in the Arctic"(SIGMA) Project in Greenland in 2011-2013, Bulletin of Glaciological Research, 32, 3–20, 2014.

Bøggild, C. E., Olesen, O. B., Andreas, P. A., and Jørgensen, P.: Automatic glacier ablation measurements using pressure transducers, Journal of Glaciology, 50, 303–304, 2004.

Box, J. E. and Steffen, K.: Sublimation on the Greenland ice sheet from automated weather station observations, Journal of Geophysical

10   Research: Atmospheres, 106, 33 965–33 981, 2001.

Braithwaite, R. J. and Olesen, O. B.: Calculation of glacier ablation from air temperature, West Greenland, in: Glacier fluctuations and climatic change, pp. 219–233, Springer, 1989.

Brock, B. W., Willis, I. C., and Sharp, M. J.: Measurement and parameterization of aerodynamic roughness length variations at Haut Glacier d'Arolla, Switzerland, Journal of Glaciology, 52, 281–297, 2006.

15   Citterio, M., van As, D., Ahlstrøm, A. P., Andersen, M. L., Andersen, S. B., Box, J. E., Charalampidis, C., Colgan, W. T., Fausto, R. S., Nielsen, S., et al.: Automatic weather stations for basic and applied glaciological research, Geological Survey of Denmark and Greenland Bulletin, pp. 69–72, 2015.

Fausto, R., van As, D., and Mankoff, K. D.: Programme for monitoring of the Greenland ice sheet (PROMICE): Automatic weather station data. Version: v03, Geological survey of Denmark and Greenland (GEUS)., https://doi.org/10.22008/promice/data/aws, 2019.

20   Fausto, R. S., Van As, D., Ahlstrøm, A. P., and Citterio, M.: Assessing the accuracy of Greenland ice sheet ice ablation measurements by pressure transducer, Journal of Glaciology, 58, 1144–1150, 2012.

Fausto, R. S., van As, D., Box, J. E., Colgan, W., and Langen, P. L.: Quantifying the surface energy fluxes in south Greenland during the 2012 high melt episodes using in-situ observations, Frontiers in Earth Science, 4, 82, 2016a.

Fausto, R. S., van As, D., Box, J. E., Colgan, W., Langen, P. L., and Mottram, R. H.: The implication of nonradiative energy fluxes dominating

25   Greenland ice sheet exceptional ablation area surface melt in 2012, Geophysical Research Letters, 43, 2649–2658, 2016b.

Fettweis, X., Box, J. E., Agosta, C., Amory, C., Kittel, C., Lang, C., van As, D., Machguth, H., and Gallée, H.: Reconstructions of the 1900–2015 Greenland ice sheet surface mass balance using the regional climate MAR model, The Cryosphere, 11, 1015–1033, https://doi.org/10.5194/tc-11-1015-2017, https://tc.copernicus.org/articles/11/1015/2017/, 2017.

Fettweis, X., Hofer, S., Krebs-Kanzow, U., Amory, C., Aoki, T., Berends, C. J., Born, A., Box, J. E., Delhasse, A., Fujita, K., et al.: GrSMB-

30   MIP: Intercomparison of the modelled 1980–2012 surface mass balance over the Greenland Ice sheet, The Cryosphere, 14, 3935–3958, 2020.

Goff, J. A. and Gratch, S.: Low-pressure properties of water-from 160 to 212° F., Trans. Am. Heat. Vent. Eng., 52, 95–121, 1946.

Harrison, R. G., Chalmers, N., and Hogan, R. J.: Retrospective cloud determinations from surface solar radiation measurements, Atmospheric Research, 90, 54–62, 2008.

35   Holtslag, A. and De Bruin, H.: Applied modeling of the nighttime surface energy balance over land, Journal of Applied Meteorology and Climatology, 27, 689–704, 1988.

Huai, B., van den Broeke, M. R., and Reijmer, C. H.: Long-term surface energy balance of the western Greenland Ice Sheet and the role of large-scale circulation variability, The Cryosphere, 14, 4181–4199, 2020.

Kokhanovsky, A., Box, J. E., Vandecrux, B., Mankoff, K. D., Lamare, M., Smirnov, A., and Kern, M.: The determination of snow albedo from satellite measurements using fast atmospheric correction technique, Remote Sensing, 12, 234, 2020.

5 Mankoff, K. D., Solgaard, A., Colgan, W., Ahlstrøm, A. P., Khan, S. A., and Fausto, R. S.: Greenland Ice Sheet solid ice discharge from 1986 through March 2020, Earth System Science Data, 12, 1367–1383, https://doi.org/10.5194/essd-12-1367-2020, 2020.

Meredith, M., Sommerkorn, M., Cassotta, S., Derksen, C., Ekaykin, A., Hollowed, A., Kofinas, G., Mackintosh, A., Melbourne-Thomas, J., Muelbert, M., Ottersen, G., Pritchard, H., and Schuur, E.: Polar Regions., In: IPCC Special Report on the Ocean and Cryosphere in a Changing Climate [H.-O. Pörtner, D.C. Roberts, V. Masson-Delmotte, P. Zhai, M. Tignor, E. Poloczanska, K. Mintenbeck, A. Alegría, M.

10 Nicolai, A. Okem, J. Petzold, B. Rama, N.M. Weyer (eds.), 2019.

Miller, N. B., Shupe, M. D., Cox, C. J., Noone, D., Persson, P. O. G., and Steffen, K.: Surface energy budget responses to radiative forcing at Summit, Greenland, The Cryosphere, 11, 497–516, 2017.

Moon, T., Tedesco, M., Andersen, J., Box, J., Cappelen, J., Fausto, R., Fettweis, X., Loomis, B., Mankoff, K., Mote, T., et al.: Greenland Ice sheet [in" State of the Climate in 2019"], Bulletin of the American Meteorological Society, 2020a.

15 Moon, T. A., Tedesco, M., Box, J., Cappelen, J., Fausto, R., Fettweis, X., Korsgaard, N., Loomis, B., Mankoff, K., Mote, T., et al.: Arctic Report Card 2020: Greenland Ice Sheet, 2020b.

Mouginot, J., Rignot, E., Bjørk, A. A., van den Broeke, M., Millan, R., Morlighem, M., Noël, B., Scheuchl, B., and Wood, M.: Forty-six years of Greenland Ice Sheet mass balance from 1972 to 2018, Proceedings of the National Academy of Sciences, 116, 9239–9244, https://doi.org/10.1073/pnas.1904242116, https://www.pnas.org/content/116/19/9239, 2019.

20 Noël, B., Berg, W. J. v. d., Wessem, J., Meijgaard, E. v., As, D. v., Lenaerts, J., Lhermitte, S., Kuipers Munneke, P., Smeets, C., Ulft, L. H. v., et al.: Modelling the climate and surface mass balance of polar ice sheets using RACMO2–Part 1: Greenland (1958–2016), The Cryosphere, 12, 811–831, 2018.

Paulson, C. A.: The mathematical representation of wind speed and temperature profiles in the unstable atmospheric surface layer, Journal of Applied Meteorology and Climatology, 9, 857–861, 1970.

25 Ryan, J., Hubbard, A., Irvine-Fynn, T. D., Doyle, S. H., Cook, J., Stibal, M., and Box, J.: How robust are in situ observations for validating satellite-derived albedo over the dark zone of the Greenland Ice Sheet?, Geophysical Research Letters, 44, 6218–6225, 2017.

Shepherd, A., Ivins, E., Rignot, E., Smith, B., van den Broeke, M., Velicogna, I., Whitehouse, P., Briggs, K., Joughin, I., Krinner, G., Nowicki, S., Payne, T., Scambos, T., Schlegel, N., Geruo, A., Agosta, C., Ahlström, A., Babonis, G., Barletta, V. R., Bjørk, A. A., Blazquez, A., Bonin, J., Colgan, W., Csatho, B., Cullather, R., Engdahl, M. E., Felikson, D., Fettweis, X., Forsberg, R., Hogg, A. E., Gallee, H., Gardner,

30 A., Gilbert, L., Gourmelen, N., Groh, A., Gunter, B., Hanna, E., Harig, C., Helm, V., Horvath, A., Horwath, M., Khan, S., Kjeldsen, K. K., Konrad, H., Langen, P. L., Lecavalier, B., Loomis, B., Luthcke, S., McMillan, M., Melini, D., Mernild, S., Mohajerani, Y., Moore, P., Mottram, R., Mouginot, J., Moyano, G., Muir, A., Nagler, T., Nield, G., Nilsson, J., Noël, B., Otosaka, I., Pattle, M. E., Peltier, W. R., Pie, N., Rietbroek, R., Rott, H., Sørensen, L. S., Sasgen, I., Save, H., Scheuchl, B., Schrama, E., Schröder, L., Seo, K.-W., Simonsen, S. B., Slater, T., Spada, G., Sutterley, T., Talpe, M., Tarasov, L., Jan van de Berg, W., van der Wal, W., van Wessem, M., Vishwakarma, B. D.,

35 Wiese, D., Wilton, D., Wagner, T., Wouters, B., and Wuite, J.: Mass balance of the Greenland Ice Sheet from 1992 to 2018, Nature, 579, 233–239, 2020.

Smeets, C. and Van den Broeke, M.: The parameterisation of scalar transfer over rough ice, Boundary-layer meteorology, 128, 339–355, 2008a.

Smeets, C. and Van den Broeke, M.: Temporal and spatial variations of the aerodynamic roughness length in the ablation zone of the Greenland ice sheet, Boundary-layer meteorology, 128, 315–338, 2008b.

Smeets, P. C., Kuipers Munneke, P., Van As, D., van den Broeke, M. R., Boot, W., Oerlemans, H., Snellen, H., Reijmer, C. H., and van de Wal, R. S.: The K-transect in west Greenland: Automatic weather station data (1993–2016), Arctic, Antarctic, and Alpine Research, 50, S100 002, 2018.

Solgaard, A., Kusk, A., Boncori, J. P. M., Dall, J., Mankoff, K. D., Ahlstrøm, A. P., Andersen, S. B., Citterio, M., Karlsson, N. B., Kjeldsen, K. K., Korsgaard, N. J., Larsen, S. H., and Fausto, R. S.: Greenland ice velocity maps from the PROMICE project, Earth System Science Data Discussions, 2021, 1–29, https://doi.org/10.5194/essd-2021-46, https://essd.copernicus.org/preprints/essd-2021-46/, 2021.

Steffen, K., Box, J., and Abdalati, W.: Greenland climate network: GC-Net, US Army Cold Regions Reattach and Engineering (CRREL), CRREL Special Report, pp. 98–103, 1996.

Swinbank, W. C.: Long-wave radiation from clear skies, Quarterly Journal of the Royal Meteorological Society, 89, 339–348, 1963.

Van As, D.: Warming, glacier melt and surface energy budget from weather station observations in the Melville Bay region of northwest Greenland, Journal of Glaciology, 57, 208–220, 2011.

Van As, D., Van Den Broeke, M., Reijmer, C., and Van De Wal, R.: The summer surface energy balance of the high Antarctic plateau, Boundary-Layer Meteorology, 115, 289–317, 2005.

van As, D., Fausto, R. S., Ahlstrøm, A. P., Andersen, S. B., Andersen, M. L., Citterio, M., Edelvang, K., Gravesen, P., Machguth, H., Nick, F. M., et al.: Programme for Monitoring of the Greenland Ice Sheet (PROMICE): first temperature and ablation records, Geological Survey of Denmark and Greenland Bulletin, 23, 73–76, 2011a.

van As, D., Fausto, R. S., and PROMICE project team, .: Programme for Monitoring of the Greenland Ice Sheet (PROMICE): first temperature and ablation records, GEUS Bulletin, 23, 73–76, 2011b.

van As, D., Fausto, R. S., Colgan, W. T., and Box, J. E.: Darkening of the Greenland ice sheet due to the meltalbedo feedback observed at PROMICE weather stations, Geological Survey of Denmark and Greenland (GEUS) Bulletin, 28, 69–72, 2013.

Van As, D., Andersen, M. L., Petersen, D., Fettweis, X., Van Angelen, J. H., Lenaerts, J. T., Van Den Broeke, M. R., Lea, J. M., Bøggild, C. E., Ahlstrøm, A. P., et al.: Increasing meltwater discharge from the Nuuk region of the Greenland ice sheet and implications for mass balance (1960–2012), Journal of Glaciology, 60, 314–322, 2014.

van As, D., Fausto, R. S., Steffen, K., et al.: Katabatic winds and piteraq storms: Observations from the Greenland ice sheet, GEUS Bulletin, 31, 83–86, 2014.

van den Broeke, M., van As, D., Reijmer, C., and van de Wal, R.: Assessing and improving the quality of unattended radiation observations in Antarctica, Journal of Atmospheric and Oceanic Technology, 21, 1417–1431, 2004.

Vandecrux, B., Mottram, R., Langen, P. L., Fausto, R. S., Olesen, M., Stevens, C. M., Verjans, V., Leeson, A., Ligtenberg, S., Kuipers Munneke, P., et al.: The firn meltwater Retention Model Intercomparison Project (RetMIP): Evaluation of nine firn models at four weather station sites on the Greenland ice sheet, The Cryosphere, 14, 3785–3810, 2020.

Vaughan, D. J. C., Allison, I., Carrasco, J., Kaser, G., Kwok, R., Mote, P., Murray, T., Paul, F., Ren, J., Rignot, E., Solomina, O., Steffen, K., and Zhang, T.: Observations: Cryosphere. In: Climate Change 2013: The Physical Science Basis., Contribution of Working Group I to the Fifth Assessment Report of the Intergovernmental Panel on Climate Change [Stocker, T.F., D. Qin, G.-K. Plattner, M. Tignor, S.K. Allen, J. Boschung, A. Nauels, Y. Xia, V. Bex and P.M. Midgley (eds.)]., 2013.

Vignola, F.: University of Oregon Solar Radiation Monitoring Laboratory., http://solardat.uoregon.edu/SolarRadiationBasics.html, 2019.
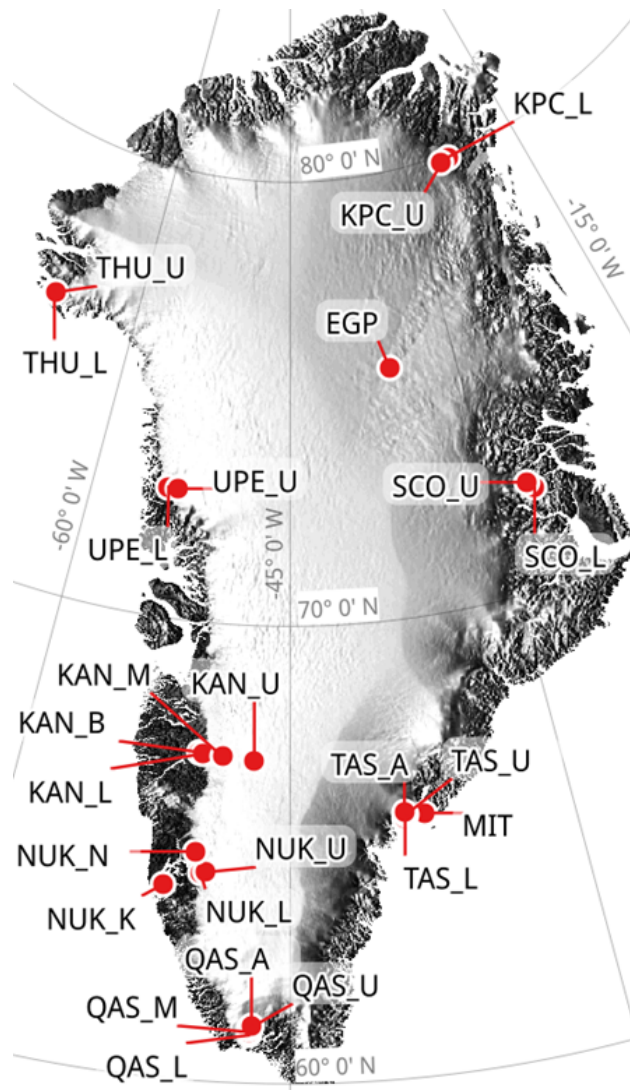
Figure 1. Map of Greenland with PROMICE automatic weather station locations.
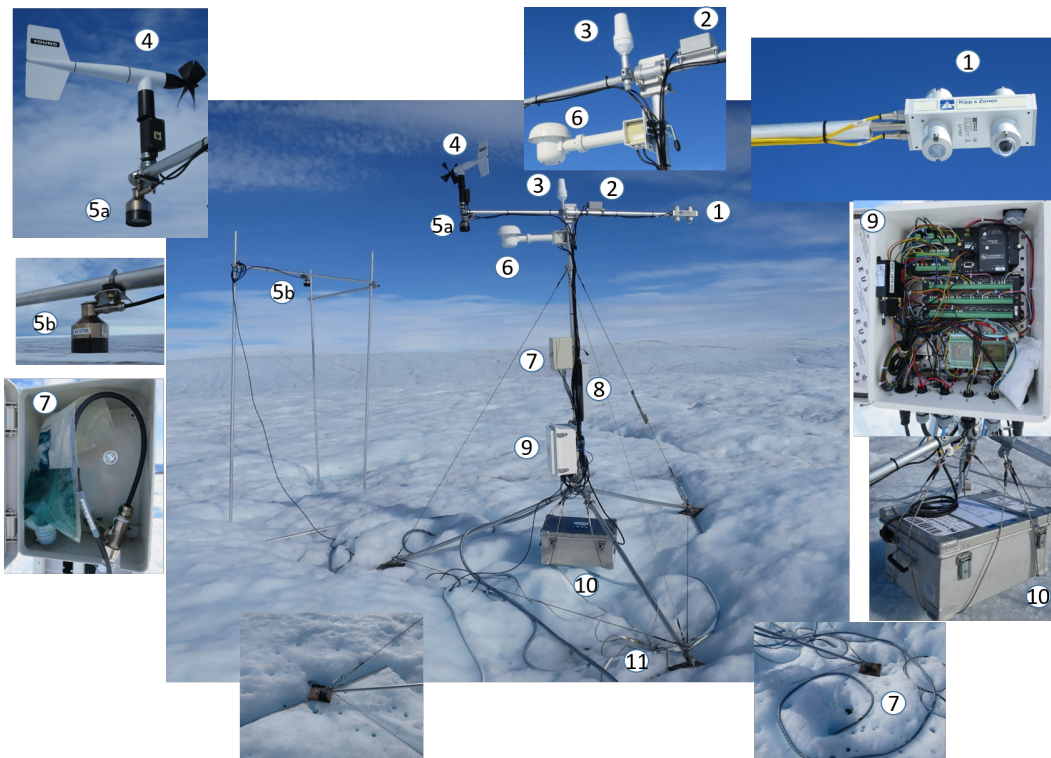
Figure 2. PROMICE automatic weather station UPE_U photographed on 4 August 2018. 1: Radiometer, 2: Inclinometer, 3: Satellite antenna, 4: Anemometer, 5: Sonic rangers, 6: Hygro-/thermometer (aspirated), 7: Pressure transducer, 8: Solar panel, 9: Data logger, multiplexer, barometer, satellite modem and GPS antenna, 10: Battery box, 11: Thermistor string (8 levels).
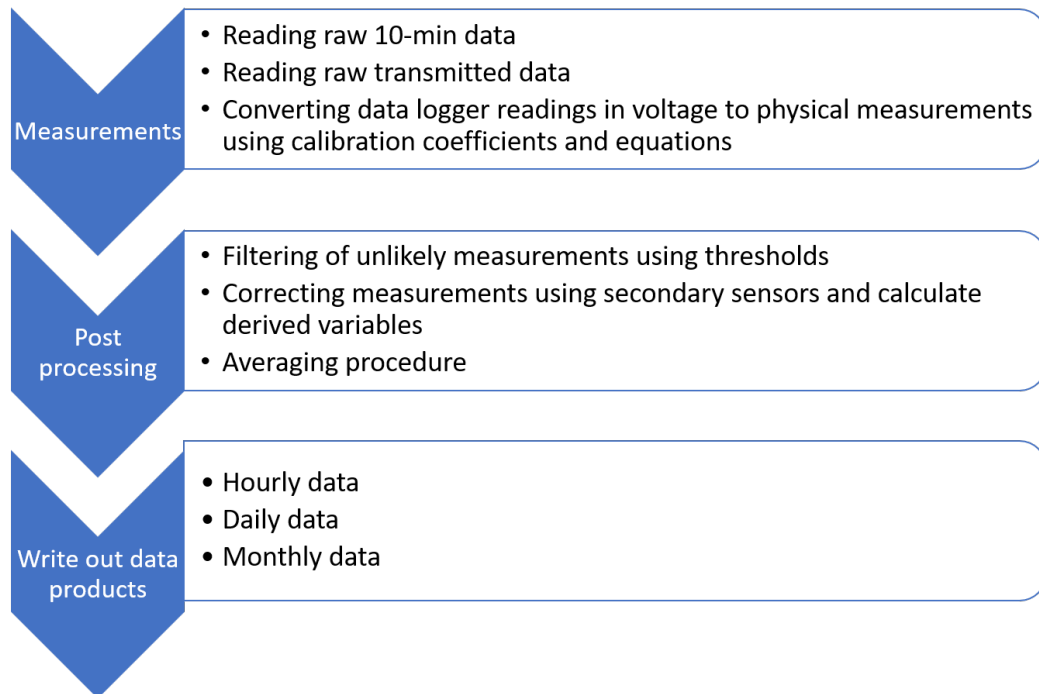
Figure 3. Illustration of the AWS data processing chain.
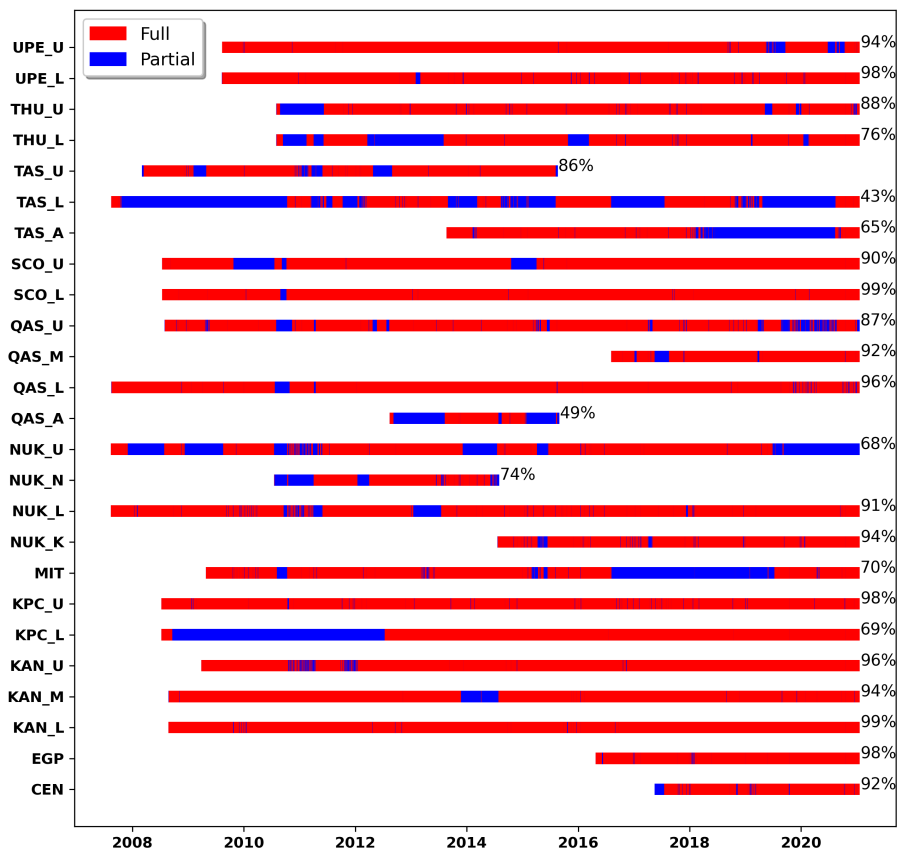
Figure 4. Combined availability of the 8 critical variables required for surface energy balance calculation from PROMICE daily products. See Appendix for data availability of each of the variables.
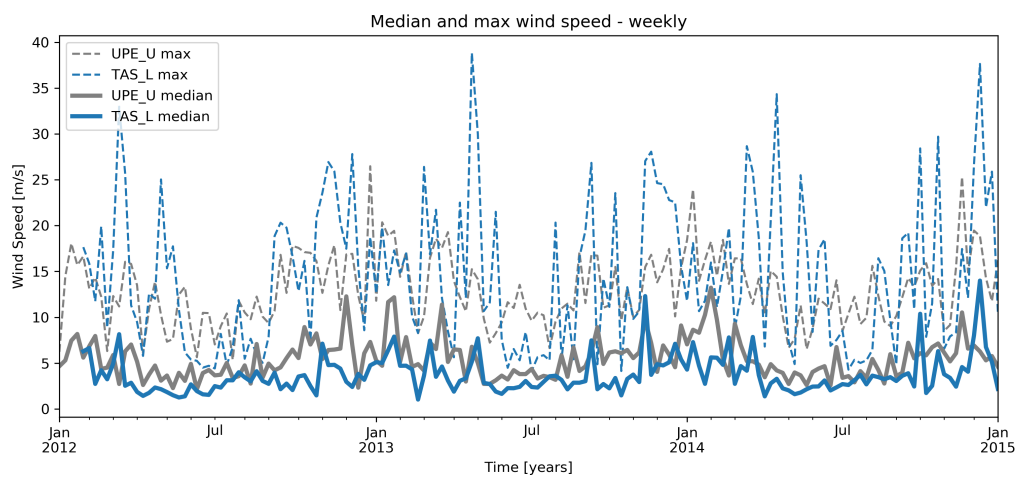
Figure 5. Weekly median wind speeds vs maximum 10-min wind speed within that week
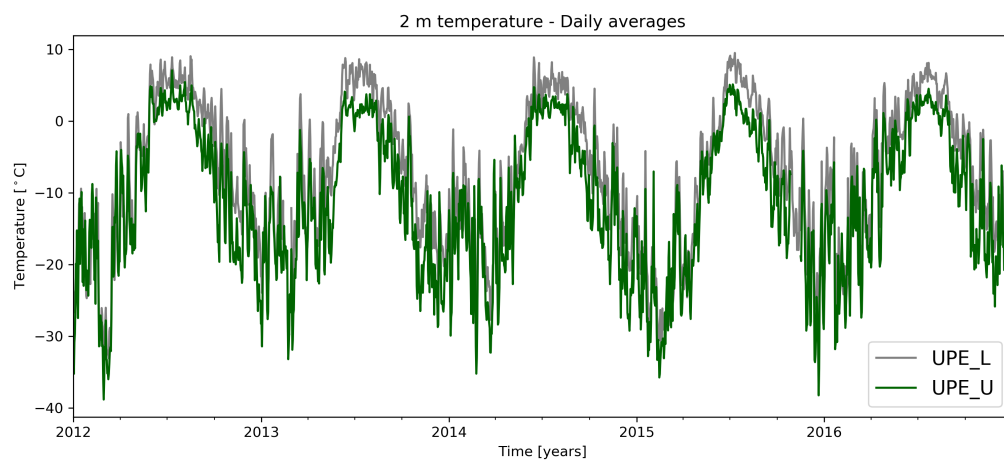
Figure 6. Daily air temperatures from UPE_L and UPE_U.
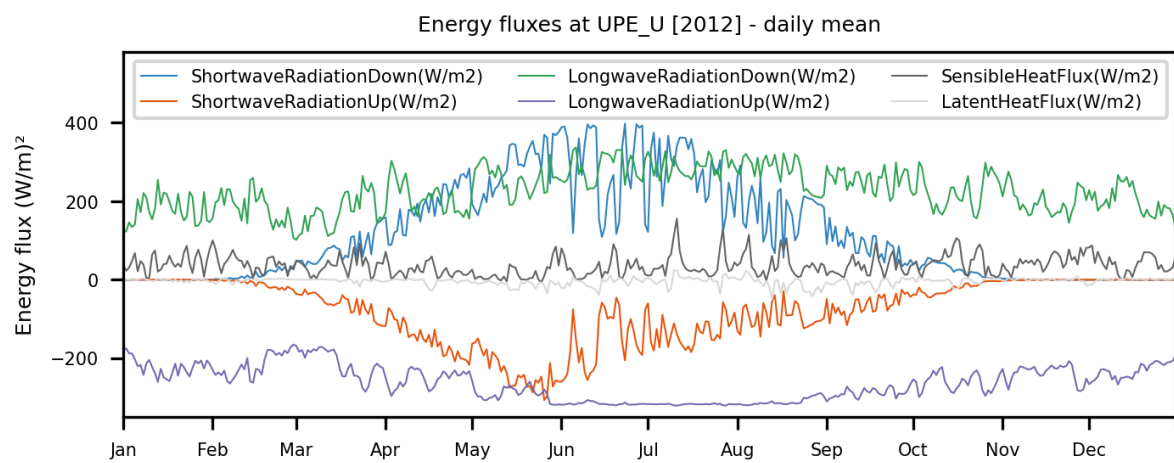
Figure 7. Estimated surface energy balance components for UPE_U.

Table 1. Metadata for the PROMICE automatic weather station network. Latitude, longitude and elevation are derived from automated GPS measurements in summer 2016, or during the last weeks of operation if discontinued.

Station name	Latitude (°N)	Longitude (°W)	Elevation (m a.s.l.)	Start date (YYYY-MM-DD)	Last Visit (YYYY-MM-DD)
KPC_L	79.9108	24.0828	370	2008-07-17	2019-07-12
KPC_U	79.8347	25.1662	870	2008-07-17	2019-07-13
EGP	75.6247	35.9748	2660	2016-05-01	2019-05-31
SCO_L	72.2230	26.8182	460	2008-07-21	2020-07-26
SCO_U	72.3933	27.2333	970	2008-07-21	2020-07-26
MIT	65.6922	37.8280	440	2009-05-03	2019-07-17
TAS_L	65.6402	38.8987	250	2007-08-23	2020-08-19
TAS_U[3]	65.6978	38.8668	570	2007-08-15	2015-08-13
TAS_A	65.7790	38.8995	890	2013-08-28	2020-08-17
QAS_L	61.0308	46.8493	280	2007-08-24	2020-08-29
QAS_M	61.0998	46.8330	630	2016-08-11	2020-09-09
QAS_U	61.1753	46.8195	900	2008-08-07	2020-08-29
QAS_A[3]	61.2430	46.7328	1000	2012-08-20	2015-08-24
NUK_L	64.4822	49.5358	530	2007-08-20	2020-08-28
NUK_U	64.5108	49.2692	1120	2007-08-20	2020-08-31
NUK_K[1]	64.1623	51.3587	710	2014-07-28	2020-08-31
NUK_N[3]	64.9452	49.8850	920	2010-07-25	2014-07-25
KAN_B[2]	67.1252	50.1832	350	2011-04-13	2020-09-10
KAN_L	67.0955	49.9513	670	2008-09-01	2020-09-09
KAN_M	67.0670	48.8355	1270	2008-09-02	2020-09-12
KAN_U	67.0003	47.0253	1840	2009-04-04	2020-09-08
UPE_L	72.8932	54.2955	220	2009-08-17	2020-08-10
UPE_U	72.8878	53.5783	940	2009-08-17	2020-08-08
THU_L	76.3998	68.2665	570	2010-08-09	2019-05-11
THU_U	76.4197	68.1463	760	2010-08-09	2019-05-11
THU_U2	76.3903	68.1101	744	2017-05-22	2019-05-11
CEN	77.1333	61.0333	1880	2017-05-25	2019-05-16

On peripheral glacier[1] On land[2] Discontinued[3]

Table 2. Instrument information, accuracy, power, and maintenance schedule. More information on each instrument is available in Appendix A.

Instrument type	Manufaturer	Model	Accuracy (Unit)	Maintenance schedule
Barometer	Campbell Scientific	CS100 / Setra 278	±2.0 (hPa)	5 years
Thermometer, aspirated	Rotronic in Rotronic assembly	MP100H-4-1-03-00-10DIN	±0.1 (K)	5 years
Hygro-/thermometer, aspirated	Rotronic in Rotronic assembly	HygroClip HC2 or HC2-S3	±0.1 (K) ±0.8% (rh)	visit
Anemometer	R.M. Young	05103-5	±0.2 (ms-1) or 1 (%) of reading	3 years
Radiometer	Kipp & Zonen	CNR1 or CNR4	±10 (%)	3 years
Sonic ranger (2)	Campbell Scientific	SR50A	±1 (cm) or ±0.4 (%) of reading	1-2 years
Pressure transducer	Ørum & Jensen in GEUS assembly	NT1400 or NT1700	±2.5 (cm)	5 years
Thermistor string	GEUS	RS PRO Termistor, 100 kΩ	±0.9 (%)	5 years
Inclinometer	HL Planar in GEUS assembly	NS-25/E2	0.6 (%)	5 years
GPS antenna	Trimble/Tallysman	SAF5270-G/TW4020	2.5 (m)	5 years
Iridium modem	NAL Research	9602-LP	-	5 years
Iridium antenna	Campbell Scientific	30741	-	5 years
Batteries (4x28 Ah)	Panasonic	LC-XC1228P	-	5 years
Solar panel	RS PRO	RS PRO 10 W	-	5 years

Table 3. PROMICE AWS average bias and average standard deviation between corrected and uncorrected incoming solar radiation derived from the daily data product.

Station name	Number of observations	Average Bias (W m^2)	Standard deviation (W m^2)
KPC_L	3332	3.56	20.52
KPC_U	3815	0.15	6.26
EGP	1415	-0.45	11.55
SCO_L	4382	-2.13	12.06
SCO_U	3965	-1.67	9.14
MIT	2579	5.08	14.29
TAS_L	2353	2.63	14.36
TAS_U	2138	-1.17	18.77
TAS_A	1682	-0.02	14.24
QAS_L	4484	-1.30	15.06
QAS_U	3997	-0.74	11.48
QAS_M	1218	-1.87	10.66
QAS_A	539	-0.85	11.43
NUK_L	4138	1.65	13.51
NUK_U	3275	2.13	15.59
NUK_N	1128	-0.21	10.04
NUK_K	2124	-0.83	41.39
KAN_L	4373	7.58	13.69
KAN_M	4153	-0.40	12.65
KAN_U	3914	5.53	16.84
UPE_L	3953	-0.33	10.62
UPE_U	3830	0.69	12.42
THU_L	2632	0.29	9.23
THU_U	3148	-0.44	7.43
CEN	955	-4.37	21.59

Table 4. PROMICE AWS displacement statistics from monthly average GPS data. There is no GPS data avilable for AWS CEN.

Station name	First valid date (YYYY-MM-DD)	Latest valid date (YYYY-MM-DD)	Time span (yr)	Displacement (m)	Displacement rate (m yr^{-1})	Elevation change (m)
KPC_L	2008-11-15	2020-06-15	11.6	80	6.9	-15
KPC_U	2008-08-15	2020-06-15	11.8	170	14.3	-2
EGP	2016-07-15	2020-06-15	3.9	150	38.2	-1
SCO_L	2008-08-15	2017-07-15	8.9	749	84.1	-14
SCO_U	2008-08-15	2012-01-15	3.4	386	112.9	-8
MIT	2009-05-15	2020-09-15	11.3	581	51.2	-31
TAS_L	2008-11-15	2020-07-15	11.7	198	17.0	-29
TAS_U	2008-11-15	2015-07-15	6.7	340	51.0	3
TAS_A	2015-09-15	2018-09-15	3.0	275	91.5	-6
QAS_L	2009-09-15	2020-06-15	10.7	120	11.1	-55
QAS_U	2008-08-15	2020-04-15	11.7	622	53.3	-21
QAS_M	2016-09-15	2020-08-15	3.9	129	32.9	-12
QAS_A	2013-09-15	2015-02-15	1.4	121	85.4	-1
NUK_L	2007-11-15	2020-07-15	12.7	1104	87.2	-69
NUK_U	2008-11-15	2020-08-15	11.7	1508	128.4	-21
NUK_N	2010-11-15	2014-07-15	3.7	84	22.9	-4
NUK_K	2015-08-15	2020-07-15	4.9	2	0.4	-8
KAN_L	2008-09-15	2020-08-15	11.9	1267	106.3	-33
KAN_M	2008-09-15	2020-08-15	11.9	1240	104.1	-1
KAN_U	2009-04-15	2020-08-15	11.3	597	52.7	-11
UPE_L	2009-09-15	2020-07-15	10.8	17	1.6	-20
UPE_U	2009-09-15	2020-07-15	10.8	2197	202.8	-62
THU_L	2014-10-15	2020-06-15	5.7	26	4.6	-6
THU_U	2016-08-15	2020-06-15	3.8	24	6.3	-2

Table 5. Threshold values used in the filtering process for each measured variable.

Variable	Units	Low threshold	High threshold
Pressure	hPa	650	1100
All temperatures	°C	-80	30
Relative humidity	%	0	100
Wind speed	$m\,s^{-1}$	0	100
Wind direction	°	0	360
Downward shortwave radiation	$W\,m^{-2}$	-10	1500
Upward shortwave radiation	$W\,m^{-2}$	-10	1000
Downward longwave radiation	$W\,m^{-2}$	50	500
Upward longwave radiation	$W\,m^{-2}$	50	500
Sensor boom height	m	0.3	3.0
Stake assembly height	m	0.3	8.0
Pressure transducer assembly	m	0	30
Boom tilt in both directions	°	-30	30
Latitude	°N	60	83
Longitude	°W	20	70
Elevation	m	0	3000
Fan current	mA	0	200
Battery voltage	V	0	30

Table 6: Short description of all the variables in our data products. An updated version of this short description is kept as a README.txt file in the data product download folder

Variable in hourly (H), daily (D) and monthly (M) data products	Units	In data product	Short description
Year	-	H, D, M	-
MonthOfYear	-	H, D, M	Month of year during which measurements are taken and averaged.
DayOfMonth	-	H, D	Day of month during which measurements are taken and averaged.
HourOfDay(UTC)	UTC	H	Hour of day during which measurements are taken and averaged.
DayOfYear	-	H, D, M	Day of year during which measurements are taken and averaged.
DayOfCentury	-	H, D, M	Day of century during which measurements are taken and averaged.
AirPressure(hPa)	hPa	H, D, M	Barometric pressure in logger enclosure.
AirTemperature(C)	°C	H, D, M	Primary air temperature. Measurement height is approximately HeightSensorBoom – 0.1 m, or 2.6 m over bare ice surfaces.
AirTemperatureHygroClip(C)	°C	H, D, M	Secondary air temperature. Measurement height is approximately HeightSensorBoom – 0.1 m, or 2.6 m over bare ice surfaces.
RelativeHumidity(%)	%	H, D, M	Relative humidity wrt water/ice above/below freezing. Measurement height is approximately HeightSensorBoom –10 cm, or 2.6 m over bare ice surfaces.
SpecificHumidity(g/kg)	g kg^{-1}	H, D, M	Calculated from RelativeHumidity.
WindSpeed(m/s)	m s^{-1}	H, D, M	Measurement height is approximately HeightSensorBoom + 0.4 m, or 3.1 m over bare ice surfaces.
WindDirection(d)	°	H, D, M	Measurement height is approximately HeightSensorBoom + 0.4 m, or 3.1 m over bare ice surfaces.
Continued on next page			

Table 6 – continued from previous page

Variable in hourly (H), daily (D) and monthly (M) data products	Units	In data product	Short description
SensibleHeatFlux(W/m2)	W m^{-2}	H, D, M	Calculated using gradients of wind speed, and temperature between the surface and measurement level. Aerodynamic surface roughness for momentum is set to 0.001 m.
LatentHeatFlux(W/m2)	W m^{-2}	H, D, M	Calculated using gradients of wind speed and humidity between the surface and measurement level. Aerodynamic surface roughness for momentum is set to 0.001 m.
ShortwaveRadiationDown(W/m2)	W m^{-2}	H, D, M	Measurement height is approximately HeightSensorBoom + 0.1 m, or 2.8 m over bare ice surfaces.
ShortwaveRadiationDown_Cor(W/m2)	W m^{-2}	H, D, M	Tilt-corrected values calculated from ShortwaveRadiationDown.
ShortwaveRadiationUp(W/m2)	W m^{-2}	H, D, M	Measurement height is approximately HeightSensorBoom + 0.1 m, or 2.8 m over bare ice surfaces.
ShortwaveRadiationUp_Cor(W/m2)	W m^{-2}	H, D, M	Tilt-corrected values calculated from ShortwaveRadiationUp.
Albedo_theta<70d	-	H, D, M	Surface albedo calculated from ShortwaveRadiationDown_Cor and ShortwaveRadiationUp_Cor using values obtained for solar zenith angles below 70°.
LongwaveRadiationDown(W/m2)	W m^{-2}	H, D, M	Measurement height is approximately HeightSensorBoom + 0.1 m, or 2.8 m over bare ice surfaces.
LongwaveRadiationUp(W/m2)	W m^{-2}	H, D, M	Measurement height is approximately HeightSensorBoom + 0.1 m, or 2.8 m over bare ice surfaces.
CloudCover	%	H, D	Estimated from LongwaveRadiationDown and AirTemperature.
SurfaceTemperature(C)	°C	H, D	Calculated from LongwaveRadiationUp and LongwaveRadiationDown. Surface longwave emissivity is set to 0.97.

Variable in hourly (H), daily (D) and monthly (M) data products	Units	In data product	Short description
HeightSensorBoom(m)	m	H, D, M	Measured at approximately 0.1 m below the sensor boom. The sensitivity of sonic ranger readings to air temperature is removed.
HeightStakes(m)	m	H, D	Measured on a boom connecting aluminum stakes drilled into ice/firn. The sensitivity of sonic ranger readings to air temperature is removed.
DepthPressureTransducer(m)	m	H, D	Typically drilled >10 m into ice, reduces as ablation occurs.
DepthPressureTransducer_Cor(m)	m	H, D	Air pressure contributions eliminated from DepthPressureTransducer.
AblationPressureTransducer(mm)	mm	D	Daily ablation estimate from pressure transducer. Only in the daily file.
IceTemperature1-8(C)	°C	H, D	Subsurface temperature installed at 1, 2, 3, 4, 5, 6, 7 and 10 m depth at ablation-area sites. Note that the thermistor strings in the ablation area will melt out.
TiltToEast(d)	°	H, D	Station tilt towards the east. Station may have rotated.
TiltToNorth(d)	°	H, D	Station tilt towards the north. Station may have rotated.
TimeGPS(hhmmssUTC) GPS time stamp.	UTC	H, D	
LatitudeGPS(degN)	°N	H, D, M	Daily and monthly averages are calculated only using HorDilOfPrecGPS values smaller than 1.
LongitudeGPS(degW)	°W	H, D, M	Daily and monthly averages are calculated only using HorDilOfPrecGPS values smaller than 1.
ElevationGPS(m)	m	H, D, M	Daily and monthly averages are calculated only using HorDilOfPrecGPS values smaller than 1.
HorDilOfPrecGPS	-	H, D	GPS horizontal dilution of precision (HDOP) value.

Variable in hourly (H), daily (D) and monthly (M) data products	Units	In data product	Short description
LoggerTemperature(C)	°C	H, D	Temperature measured by the data logger in the enclosure at 1-1.5 m above the bare ice surface.
FanCurrent(mA)	mA	H, D	Current drawn for ventilation of the temperature and humidity assembly. Normal values exceed 100 mA.
FanOK(%)	%	M	Percentage of time with sufficient ventilation of the temperature and humidity assembly. Only in the monthly file.
BatteryVoltage(V)	V	H, D	Voltage of the four 28 Ah batteries. Ventilation of the temperature and humidity assembly, and GPS positioning, stop below 11.5 V.

Appendix A: Sensor tables

A1   Instrument information, accuracy, and power consumption

A1.1   Barometer

Table A1. Barometer: details from the manufacturer for Setra CS100 Barometric pressure sensor (Model 278).

Parameter	Value	Unit
Measurement Range	600 – 1100	mb
Operating Temperature Range	–40 to 60 (–40 to 140)	°C (°F)
Storage Temperature Range	–60 to 120 (–76 to 248)	°C (°F)
Proof Pressure	1500	mb
Burst Pressure	2000	mb
Humidity Range non-condensing	(up to 95%)	RH
Media Compatibility non-corrosive, non-condensing air or gas Resolution:	0.01	mb
Total Accuracy:	±0.5 @ 20 °C	mb
	±1.0 @ 0 to 40 °C	
	±1.5 @ –20 to 50 °C	
	±2.0 @ –40 to 60 °C	
Linearity	±0.4	mb
Hysteresis	±0.05	mb
Repeatability	±0.03	mb
Long-term Stability:	±0.1 per year	mb

Thermometer and Hygrometer

Rotronic MP102H with Pt100 (±0.1 K) and HC2-S3 (or HC2) probe (±0.1 K, ± 0.8% rh, at 23°C ± 5 K), housed in a RS12T aspirated shield. Accuracy and factory measurement error of Rotronic probes: The Rotronic system uses ventilated weather and

Table A2. Thermometer and hygrometer: details from the manufacturer Rotronics.

Probe type	Thermometer	Hygrometer	
Pt100	±0.1 K	-	
HC2-S3	±0.1 K	± 0.8% rh	at 23°C ± 5 K
HC2	±0.1 K	± 0.8% rh	at 23°C ± 5 K

radiation shields RS12T with a 12 VDC fan. Due to the white housing of the radiation shield, the influence of thermal radiation on the measurements of temperature and humidity is reduced to a minimum. The shield also offers optimum protection in stormy weather, even against horizontally driven rain and snow. The fan is supplied by a separate cable.

Anemometer

Table A3. Anemometer: details from the manufacturer Young, model 05103.

	Wind Speed	
Parameter	**Value**	**Unit**
Range	0-50 (0-112) m/s (mph)	
Accuracy	±0.2 (±0.4) or 1% of reading	m/s (mph)
Starting threshold	0.4 (0.9)	m/s (mph)
Distance constant	2.1 (6.9), 63% recovery	m (ft)
Output	ac voltage (three pulses per revolution)	
90 Hz (1800 rpm) = 9.2 m/s (20.6 mph)		
Resolution	(0.1024 m s-1) / (scan rate in seconds)	
	Wind Direction	
Parameter	**Value**	**Unit**
Mechanical range	0-360	°
Electrical range	355 (5 open)	°
Accuracy	±3	°
Starting threshold	0.5 (1.0) at 10° displacement	m/s (mph)
Distance constant	1.2 (3.9), 50% recovery	m (ft)
Damping ratio	0.45	
Damped Natural Wavelength	4.9 (16.1)	m (ft)
Undamped Natural Wavelength	4.4 (14.4)	m (ft)
Output	Analog dc voltage from potentiometer (resistance 10 kOhm). Linearity is 0.25%. Life expectancy is 50 million revolutions.	
Voltage	Power switched excitation voltage supplied by datalogger.	

Radiometer

Kipp & Zonen CNR1 and CNR4. CNR4 is a four-component net radiometer for accurate and reliable measurements. There are four separate signal outputs and the integrated temperature sensors can be used to calculate the net radiation. The CNR4 combines two pyranometers for solar radiation with two pyrgeometers for infrared measurements. The upper pyrgeometer has a silicon meniscus dome so that water rolls off and the field of view is 180 °. The design is lightweight and the white sun shield reduces solar heating of the instrument body. Although similar to CNR4, the older CNR1 has a slightly different instrument body and measurement range (see Tables below), but perform with similar accuracy. We do not flag the products with respect to which instrument type we used for that each station setup. We therefore assume the same accuracy for both CNR1 and CNR4. Kipp & Zonen's CM3 ISO-class, thermopile pyranometer, CG3 pyrgeometer, PT100 RTD

Table A4. Thermometer and Hygrometer: details from the manufacturer Rotronics.

Parameter	Value	Value	Unit
Sensors	CNR 1	CNR 4	
Pyranometer Spectral Response	305 to 2800	305 to 2800	nm
Pyrgeometer Spectral Response	5000 to 50,000	4500 to 42,000	nm
Response Time	18	< 18	S
Temperature Dependence of Sensitivity	-	< 4 (-10° to +40°C)	%
Sensitivity Range	7 to 15	5 to 20	μ V W^{-1} m^2
Pyranometer Output Range	0 to 25	0 to 15	mV
Pyrgeometer Output Range	±5	±5	mV
Expected Accuracy for Daily Totals	±10	±10	%
Non-Linearity	-	< 1	%

Thermistor

Table A5. Thermistor: details from the manufacturer. Fabricated at GEUS, the thermistor strings are based on resistors.

Parameter	Value	Unit
Maximum Operating Temperature	+150	°C
Minimum Operating Temperature	-80	°C
Resistance @ 25 °C	100	kω
Temperature Coefficient Type	NTC	
Thermal Time Constant	10	S
Tolerance	±0.9	%

Inclinometer

Table A6. Inclinomter: details from the manufacturer HL planar Technik model NS-25/E2.

Parameter	Value	Unit
Measuring range	± 25	°
Measuring axes	Two (x/y) orthogonal orientated	
Resolution	0.002	°
Precision	0.6	%
Banking sensitivity	< 1.5	%
Temperature stability:		
Zero point	0.002	K
Sensitivity	0.005	K

Sonic rangers

The accuracy of the SR50A sonic ranger given by the manufacturer (Campbell Scientific) is ± 1 cm or ± 0.4% of the measuring height after temperature correction.

Pressure transducer

5   The PROMICE AWSs are equipped with an Ørum & Jensen NT1400/NT1700 pressure transducer assembly (PTA). The PTA monitor ice surface height change due to ablation. The pressure transducer sensor has an accuracy of 2.5 cm given by the manufacturer (Ørum & Jensen Elektronik A/S).

GPS

We have equipped a single frequency GPS. It is built into Iridium 9602-LP modem. The Manufacturer describe the Receiver
10   Type in the following way: NEO-6Q, 1575.42 MHz (L1), 16-channel, C/A code Accuracy: 2.5 m CEP, Update Rate: 5 Hz, Start-up Times: 1 second hot-starts, 28 seconds warm- and cold-starts Sensitivity: -160 dBm

Appendix B: Station climatology

Table B1: Average (AVG) and standard deviation (STD) for meteorogical variables and surface energy balance components derived from the daily products: Air pressure (AP), air temperature (AT), relative humidity (RH), wind speed (WS), sensible heat flux (SHF), latent heat flux (LHF), incoming solar radiation (SRI), outgoing solar radiation (SRO), incoming longwave radiation (LRI), and outgoing longwave radiation (LRO). Sign convention: Negative fluxes remove energy from the surface, while positive fluxes add energy to the surface. This table supplements Figure 4.

Station name	Variable Unit	AP (hPa)	AT (°C)	RH (%)	WS (ms^{-1})	SHF (Wm^{-2})	LHF (Wm^{-2})	SRI (Wm^{-2})	SRO (Wm^{-2})	LRI (Wm^{-2})	LRO (Wm^{-2})
CEN	AVG	792.0	-22.0	95.4	5.8	9.4	-3.4	147.5	-119.9	204.3	-228.0
	STD	11.2	12.7	5.4	2.7	13.5	7.0	145.0	117.4	38.5	44.9
EGP	AVG	718.5	-27.6	96.6	5.3	8.5	-0.9	157.7	-125.8	184.5	-208.4
	STD	10.9	13.7	4.2	2.0	10.6	3.5	141.8	114.2	36.9	45.0
KAN_L	AVG	927.1	-7.1	76.5	4.5	28.0	-10.7	131.2	-79.0	238.3	-277.1
	STD	10.6	9.5	11.4	2.3	27.3	16.4	123.0	70.5	45.3	37.1
KAN_M	AVG	859.4	-11.7	85.0	6.1	20.7	-7.1	139.2	-97.5	224.8	-262.3
	STD	11.0	10.2	13.9	3.1	20.1	11.2	127.4	89.4	44.3	40.9
KAN_U	AVG	799.1	-14.8	89.2	6.7	16.0	-7.9	160.8	-128.2	216.0	-251.8
	STD	11.5	10.5	7.4	3.5	17.2	12.5	134.4	104.3	43.0	40.8
KPC_L	AVG	966.5	-13.3	76.1	5.9	27.7	-9.7	118.0	-74.3	211.4	-252.7
	STD	9.4	11.4	10.8	2.7	25.1	12.6	132.4	87.8	49.7	45.3
KPC_U	AVG	905.8	-17.1	84.7	4.9	20.9	-5.5	128.8	-99.4	205.8	-241.9
	STD	9.6	12.0	8.8	2.2	17.7	9.7	142.9	110.0	45.0	46.8
MIT	AVG	952.7	-2.7	78.7	3.2	20.3	-4.2	126.2	-72.5	266.6	-292.9
	STD	13.1	5.9	16.1	2.5	16.2	12.2	123.4	78.2	38.4	26.6
NUK_K	AVG	921.6	-4.6	77.9	2.7	18.7	-6.2	110.0	-66.1	258.8	-285.8
	STD	10.9	8.1	19.5	1.7	22.8	16.0	110.0	68.9	41.7	32.0
NUK_L	AVG	941.8	-3.5	68.8	3.4	31.4	-12.4	126.5	-59.8	253.1	-288.1
	STD	11.1	8.1	15.6	2.2	27.3	19.8	116.0	55.5	47.9	32.3
NUK_N	AVG	898.6	-7.4	77.6	4.3	19.2	-13.2	148.3	-90.6	244.2	-277.7
	STD	11.5	8.4	11.3	3.3	19.1	15.9	124.8	82.7	48.0	36.0
NUK_U	AVG	875.1	-7.4	77.2	5.3	32.5	-12.1	123.7	-86.2	239.7	-274.7
	STD	11.0	8.4	12.3	3.2	29.7	18.0	117.0	77.6	48.2	34.9

Table B1 – continued from previous page

Station name	Variable Unit	AP (hPa)	AT (°C)	RH (%)	WS (ms^{-1})	SHF (Wm^{-2})	LHF (Wm^{-2})	SRI (Wm^{-2})	SRO (Wm^{-2})	LRI (Wm^{-2})	LRO (Wm^{-2})
QAS_A	AVG	883.5	-7.7	84.8	5.8	27.0	-11.3	122.1	-88.6	243.2	-277.5
	STD	11.8	7.9	11.3	2.9	18.0	13.7	113.0	80.7	46.5	32.1
QAS_L	AVG	971.5	-1.5	72.7	4.4	35.4	-9.9	130.2	-61.1	262.9	-296.2
	STD	12.1	6.2	13.1	3.2	36.8	21.6	111.2	60.9	46.7	26.0
QAS_M	AVG	930.5	-4.4	79.4	5.8	34.3	-14.6	132.3	-81.4	255.6	-290.1
	STD	11.3	6.8	14.3	2.8	24.8	19.8	107.8	73.1	46.4	28.6
QAS_U	AVG	899.4	-6.0	84.4	5.1	27.4	-7.7	130.1	-87.8	248.0	-282.7
	STD	12.0	7.3	14.2	3.1	19.9	13.4	117.5	79.8	47.7	31.1
SCO_L	AVG	955.2	-8.0	67.5	2.8	27.6	-8.3	113.1	-58.5	233.9	-270.1
	STD	10.5	9.3	13.9	1.8	20.1	10.6	118.5	60.6	46.8	40.2
SCO_U	AVG	895.1	-9.9	69.9	4.9	33.1	-11.1	128.3	-79.0	218.6	-264.8
	STD	10.3	9.5	11.3	1.5	20.1	12.7	127.3	80.1	46.4	39.8
TAS_A	AVG	900.8	-5.9	82.9	5.0	21.0	-11.3	121.0	-82.9	257.8	-285.6
	STD	18.3	6.8	12.1	4.5	19.4	15.8	124.5	84.9	36.1	27.1
TAS_L	AVG	976.3	-2.4	80.0	3.4	25.5	-10.0	124.4	-65.8	269.0	-296.3
	STD	14.1	5.2	13.3	4.0	31.9	20.3	119.1	68.6	37.7	23.2
TAS_U	AVG	938.2	-4.1	82.6	3.5	16.8	-6.8	116.6	-73.1	263.3	-290.0
	STD	13.5	6.0	11.9	4.3	19.7	14.5	116.1	73.7	38.8	25.3
THU_L	AVG	940.3	-10.3	78.3	6.4	24.8	-7.9	121.5	-78.3	225.2	-263.0
	STD	10.2	10.4	14.9	3.8	22.6	14.3	125.2	84.6	50.5	43.5
THU_U	AVG	915.8	-12.3	84.6	6.3	25.3	-4.4	120.5	-88.3	221.6	-258.0
	STD	12.0	10.5	14.5	3.5	23.7	11.6	126.8	93.6	49.1	42.6
UPE_L	AVG	982.7	-7.1	76.5	3.5	28.7	-5.2	115.6	-77.0	244.3	-273.0
	STD	10.3	10.0	13.4	2.6	33.5	12.3	118.9	78.4	47.7	40.8
UPE_U	AVG	894.7	-10.9	79.0	5.9	35.2	-8.5	120.0	-83.5	218.0	-262.1
	STD	10.8	10.2	9.5	3.0	24.3	12.7	127.9	88.4	49.4	41.5